

Noble-metal dark-edge fermiology: Centrifugal barriers, core-hole memory, and the Zeeman Auger effect

J. C. Woicik^{1,*}, E. L. Shirley², C. Weiland¹, A. K. Rumaiz³, C. A. Cardot⁴, J. J. Kas⁴, and J. J. Rehr⁴

¹Material Measurement Science Division, Material Measurement Laboratory,

National Institute of Standards and Technology, Gaithersburg, Maryland 20899, USA

²Sensor Science Division, Physical Measurement Laboratory, National Institute of Standards and Technology, Gaithersburg, Maryland 20899, USA

³National Synchrotron Light Source II, Brookhaven National Laboratory, Upton, New York 11973, USA

⁴Department of Physics, University of Washington, Seattle, Washington 98195, USA



(Received 17 May 2021; revised 5 December 2021; accepted 7 December 2021; published 20 December 2021)

Gold and platinum both have the face-centered cubic crystal structure and are considered noble metals, yet they differ by one in atomic number. Near-edge $M_{4,5}$ x-ray absorption and resonant $M_{4,5}N_{6,7}N_{6,7}$ Auger spectra reveal “dark” edges and a photon-energy dependence of Auger electron ($4f^{12}$ final-state) energy distributions. These findings are a direct consequence of the delayed onset of $d \rightarrow f$ transitions and space quantization of the $3d$ core hole prepared by photoexcitation that is predominantly $d \rightarrow p$ vs $d \rightarrow f$ near the edge, in agreement with theoretical predictions. This study showcases the centrifugal barrier for f -wave electrons and spectral evolution arising from the existence of multiple intermediate-state channels and final states for both photoexcitation and Auger decay.

DOI: [10.1103/PhysRevB.104.245131](https://doi.org/10.1103/PhysRevB.104.245131)

I. INTRODUCTION

Matrix elements and selection rules are ubiquitous in the interaction of radiation with matter. The most celebrated is undoubtedly the dipole matrix element,

$$\langle \psi_f | \boldsymbol{\varepsilon} \cdot \mathbf{r} | \psi_i \rangle. \quad (1)$$

Here ψ_i and ψ_f are electron initial and final states, \mathbf{r} is an electron coordinate, and $\boldsymbol{\varepsilon}$ is the electric field polarization vector. In core-excitation spectroscopies, and for the special case of linearly polarized radiation with $\boldsymbol{\varepsilon}$ taken along the z axis, the spherical harmonic property of the dipole operator $\boldsymbol{\varepsilon} \cdot \mathbf{r} \propto Y_{1,0}(\theta, \phi)$ requires that the z component of orbital angular momentum l ($m = l_z$) and total angular momentum j (with $\mathbf{j} = \mathbf{l} + \mathbf{s}$ and $j_z = l_z + s_z$, \mathbf{s} being the spin angular momentum) are unchanged [1]. Moreover, a transition is only allowed if l changes to $l-1$ (“step-down” transition) or $l+1$ (“step-up” transition). Such restrictions on angular momenta and quantization of its z component, referred to as space quantization, are readily generalized to many-electron atoms [2]. If Eq. (1) is squared and multiplied by the energy-conserving density of final states, one obtains the differential cross section for the photoelectric effect, which is an example of Fermi’s golden rule [1].

One may use the above simple facts to interpret spectral signatures of the fermiology (here, denoting the study of all electronic states) for low-lying unoccupied bands in Au and Pt. This work is likely the most detailed high-resolution analysis of $M_{4,5}$ edges of these systems. The fermiology causes

“dark” M_4 and M_5 x-ray edges (where dark is synonymous with dipole transitions having weak oscillator strengths), because of centrifugal barriers delaying $3d$ - εf transitions, as a function of continuum energy ε relative to weaker $3d \rightarrow \varepsilon p$ transitions. Our study demonstrates how the j and j_z values of a $3d$ photohole retain a memory of how it was prepared that is manifested in the final-state Auger electron energy distribution, referred to here as a “Zeeman Auger” effect. This memory is responsible for a photon-energy dependence of the $M_5N_{6,7}N_{6,7}$ Auger electron energy distribution.

It should be emphasized that the present analysis of Auger spectra departs from traditional studies of postcollision interaction and the resonant-Auger effect, because the effects observed here are observed in our “noninteracting” Auger spectra, and they therefore do not arise from the Coulomb interaction of the photoelectron with either the Auger electron or the core hole [3–7]. Rather, they depend on the symmetry of the outgoing photoelectron itself. Our findings also differ from coincidence experiments that require numerous electron analyzers [8]; instead, they exploit the geometry found at many current synchrotron beamlines: an electron analyzer collects electrons within a narrow angular cone centered around the incident x-ray electric field polarization. Therefore, information stored in the core-hole memory implanted by the x-ray photon is optimally communicated to the analyzer within the Auger electron energy distribution.

II. EXPERIMENTAL METHODOLOGY

Experiments were performed at the National Institute of Standards and Technology beamline SST-2 at the National Synchrotron Light Source II, Brookhaven National

*woicik@bnl.gov

Laboratory, on 200-nm-thick Au and Pt sputter-deposited films. X-ray absorption spectra (XAS) were collected by monitoring sample drain current (total electron yield) vs incident photon energy in the vicinity of Au and Pt spin-orbit-split M_5 and M_4 edges (2207 and 2293 eV for Au, 2122 and 2203 eV for Pt). The spectra were normalized to incident photon flux determined by photocurrent from either an Al foil or a Ni mesh upstream of the sample. Auger electron spectra (AES) were recorded with a hemispherical electron analyzer operating in angular mode with a pass energy of 200 eV [9]. The total experimental resolution was better than 0.2 eV at these photon energies, and the counting statistics achieved were better than 2% for all spectra. The acceptance cone of the analyzer ($\pm 3.5^\circ$) was aligned parallel to the x-ray polarization vector of the synchrotron beam, which defines the z axis throughout this work. Samples were held at normal and glancing incidence for XAS and AES measurements, respectively. We used a liquid-nitrogen cooled, double-crystal Si(111) monochromator, specifically designed to operate close to 90° Bragg angle with an energy reproducibility better than 0.1 eV. Details of the beamline, vacuum system, and experimental procedures are given elsewhere [10–13].

III. THEORETICAL METHODOLOGY

The electronic structures and XAS of solid Au and Pt were calculated within density-functional theory (DFT) and Bethe-Salpeter equation frameworks [14]. The local-density approximation (LDA) was used in a plane-wave, pseudopotential framework. Details of the DFT calculations are given elsewhere [15]. We used hard norm-conserving pseudopotentials of the Hamann-Schlüter-Chiang type [16] with Vanderbilt cutoff functions [17], with $5s$, $5p$, $5d$, and $5f$ electrons in the valence category. We used a 100-Ry cutoff for the Bloch states. For the partial densities of states (PDOS), we used an 8000 k -point grid in the full Brillouin zone. Throughout this work, k -point grids were shifted to break degeneracies of stars of k points, thereby accelerating convergence.

For the Bethe-Salpeter calculations, we included the main corrections to the unoccupied LDA band structure, namely a 5% stretch of the energy scale. Such an enhancement of the energy scale of low-lying unoccupied bands is typical, and our 5% estimate follows from a quasiparticle treatment of a similar system by Marini *et al.* [18]. Bethe-Salpeter calculations were performed using OCEAN [14,19–21] with 145 bands total (including the $5s$ and $5p$ bands) and Brillouin-zone grids with 1728 k points. This proved that results are converged with respect to k -point sampling at 1728 k points. Sparser zone sampling was used when calculating partial absorption spectra obtained for individual core levels, because broadening effects greatly accelerated convergence. We simulated the randomized crystallographic orientation of the sputtered films by 26-point Lebedev cubature of the orientation of the sample coordinate system [22]. The x-ray electric field polarization was always along z .

The electron-hole interaction changed XAS spectra only slightly, consistent with the strong core-hole screening expected in such systems [23]. By omitting the small *multipolar* parts of the electron–core-hole interaction, we could separately calculate XAS for each $3d$ hole state with quantum

numbers j and j_z . We also confirmed that the photoelectron–core-hole interactions did not affect the Auger results significantly, other than changing the overall Auger yield in much the same way as the absorption spectrum.

For the Auger spectrum calculations, atomic structure, core-level wave functions and energies, and final-state two-hole states were obtained using a relativistic, Hartree-Fock atomic program with a dense radial grid [24]. Calculations were performed using both the Dirac equation, including determination of spin-orbit splitting, and the scalar-relativistic Koelling-Harmon equation [25] plus spin-orbit interaction in a Pauli two-component framework. This methodology used limited configuration interaction, including all states with two $N_{6,7}$ holes and mixed coupling. The level scheme agrees with observed spectra and even features anomalous ordering of levels with different total J for the same (nominal) L and S .

Auger electron continuum states were treated in a spin-orbit averaged scalar-relativistic framework. Because of the small (7° full cone) solid angle for acceptance by the electron analyzer, all spin and orbital angular momenta are quantized along that direction. Therefore, it was only necessary to consider final states with Auger electron $l_z = 0$. It was necessary to consider all possible Auger electron angular momentum and spin values, with only its l_z being known. Several selection rules play a role in determining allowed transitions and/or allowed observed final states for a given M_5 core hole in the intermediate state. It was only necessary to consider Auger electrons with orbital angular momentum l_a restricted according to $0 \leq l_a \leq 2 + 3 + 3 = 8$. (Not surprisingly, we observed that spectra were dominated by values of l_a nearest the middle of that range.) By virtue of parity, only even values of l were allowed. Also, because the final-state value of $|J_z|$ in the two-hole final state could not exceed the corresponding value of J , the triangle rule ensured additional selection rules in some cases. For instance, a two-hole final state with $J = 0$ would also have $J_z = 0$, possible only for M_5 holes with $j_z = \pm 1/2$, which would be transferred to the Auger electron. Figure 1 shows the relative contributions to the Auger spectrum for a core hole in each level at the M_4 and M_5 edges. The level schemes betrayed by these partial spectra are presented in Table I.

Theoretical $M_{4,5}N_{6,7}N_{6,7}$ Auger spectra in the solid were obtained by calculating the energy distribution for collected Auger electrons for each j and j_z of the core hole and weighting each distribution by the probability of vacating each $3d$ state as a function of photon energy. Allowed values of j_z depend on j and the photoelectron final state l as shown schematically in the form of a Zeeman diagram in Fig. 2. The probabilities also result from the PDOS and transition matrix elements that involve the Bloch states, and the pertinent Gaunt and Clebsch-Gordan coefficients. The rate at which a core level with orbital angular momentum l_c , total angular momentum $j = l_c + 1/2$ (so that $2j = 2l_c + 1$) and $j_z = m$ is vacated by photoexcitation into a partial wave channel (and neglecting spin-orbit effects in such channels) with orbital angular momentum l is given by

$$S_l(j, m) = \frac{C_l(E)}{2l_c + 1} \{ (j + m)[g(l, m - 1/2; 1, 0; l_c, m - 1/2)]^2 + (j - m)[g(l, m + 1/2; 1, 0; l_c, m + 1/2)]^2 \}. \quad (2)$$

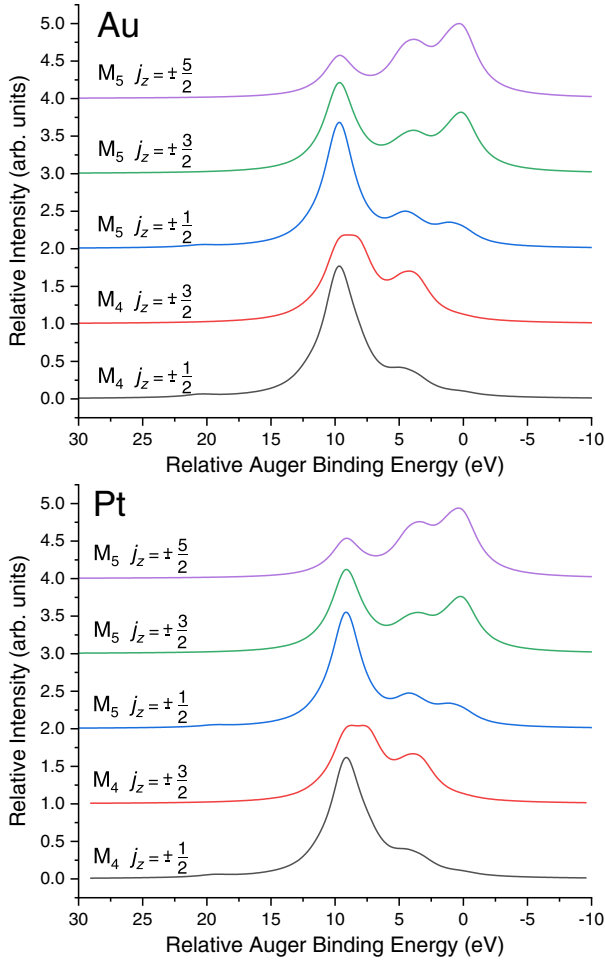


FIG. 1. Partial Auger emission spectra, with the relative binding energy of the Auger electron set to zero for the 3H , lowest-energy $4f^{12}$ two-hole final state on the core-excited site. The level schemes are shown in Table I.

TABLE I. Level schemes for the $4f^{12}$ two-hole final states. The $J = 6$, nominally 3H binding energy (B.E.) is set to zero. Despite being in the intermediate-coupling regime, the nominal term designations are provided for Hund's rule, lowest-energy state, "anti-Hund's rule" highest-energy state, and the tallest peak in all spectra.

Relative B.E. (eV)		J	Nominal term
Au	Pt		
0.00	0.00	6	3H
1.14	1.18	4	n/a
3.21	3.56	5	n/a
4.04	4.25	2	n/a
4.30	4.69	4	n/a
4.67	5.06	3	n/a
7.35	8.06	4	n/a
7.79	8.30	2	n/a
9.11	9.53	0	n/a
9.12	9.67	6	1I
9.99	10.58	1	n/a
11.19	11.99	2	n/a
19.37	20.45	0	1S

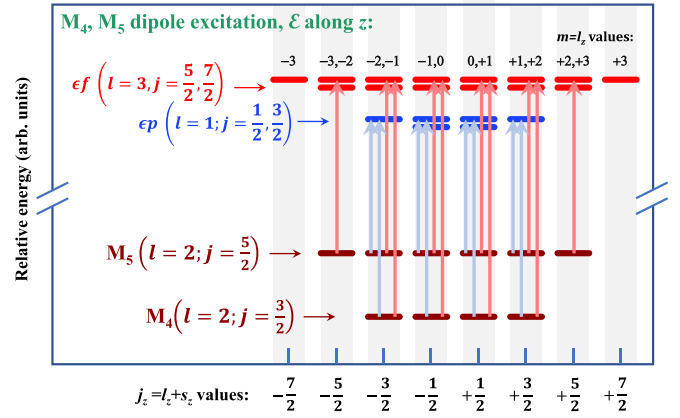


FIG. 2. Dipole-allowed Zeeman-like transitions for ϵ along z for $d \rightarrow f$ (red) and $d \rightarrow p$ (blue) core-hole excitations from the M_4 and M_5 subshells (brown). Spin-orbit splitting of the $3d$ subshell and modest spin-orbit effects in the continuum states at energy ϵ are indicated. Excitation of $m = \pm 1/2$ and $\pm 3/2$ electrons is always allowed, whereas excitation of $m = \pm 5/2$ electrons is only allowed for $d \rightarrow f$ transitions.

Here we have Gaunt coefficients given by

$$g(l_1, m_1; l_2, m_2; l_3, m_3) = \int d^2\Omega Y_{l_1, m_1}^*(\Omega) Y_{l_2, m_2}(\Omega) Y_{l_3, m_3}(\Omega). \quad (3)$$

(One is to understand $g = 0$ if there is any $|m_i| > l_i$.) The factor $C_l(E)$ includes effects of the orientationally averaged, unoccupied PDOS, radial integrals involving wave functions that are found in transition matrix elements, and all other kinematical factors. In the present case, relative ratios of values of $S_l(j, m)$ for different values of m are given by

$$S_1\left(\frac{5}{2}, \pm\frac{1}{2}\right) : S_1\left(\frac{5}{2}, \pm\frac{3}{2}\right) : S_1\left(\frac{5}{2}, \pm\frac{5}{2}\right) \\ = 3 : 2 : 0 \cong 1.000 : 0.667 : 0.000 \quad (4)$$

and

$$S_3\left(\frac{5}{2}, \pm\frac{1}{2}\right) : S_3\left(\frac{5}{2}, \pm\frac{3}{2}\right) : S_3\left(\frac{5}{2}, \pm\frac{5}{2}\right) \\ = 43 : 37 : 25 \cong 1.000 : 0.860 : 0.581. \quad (5)$$

Hence, a p -to- f crossover in the unoccupied PDOS emphasizes larger absolute values of j_z .

For a core hole with each value of m , the *partial* energy distribution curve for Auger electrons emitted into the z direction involves the factor

$$J_m(\epsilon_a) = \sum_k \sum_{l_a, m_a, \sigma_a} \left(\frac{2l_a + 1}{4\pi} \right) \\ \times \left| \sum_{ij} C_{k, ij}(\epsilon_a, l_a, m_a, \sigma_a; j, m) |V_{ee}| ij \right|^2 \\ \times \delta(E_k + \epsilon_a - \epsilon'). \quad (6)$$

Summation over k runs through the stationary, two-hole final states on the core-excited site, each with energy E_k .

Summation over i and j sums over two-hole microstates, each mixed with coefficient $C_{k,ij}$ in a stationary state k . The operator and matrix element involve the electron-electron Coulomb interaction V_{ee} . Each Auger electron has its continuous energy a and discrete quantum numbers l_a , m_a , and σ_a (again neglecting spin-orbit effects).

In a highly simplified picture, the delta function in Eq. (6) ensures energy conservation in the *overall final state*. The energy ϵ' accounts for the inner core-level binding energy and energy sharing between the photoelectron and core-excited site. More generally, the delta function should be replaced with a Lorentzian, or, even better, the resonant Auger process should be treated such as is done by Drube *et al.* [26]. In the absence of such complications, which we reasonably neglect here, the *total* energy distribution curve for Auger electrons is given by

$$I(\epsilon_a) = \sum_l \sum_m S_l(j, m) J_m(\epsilon_a). \quad (7)$$

The *shape* of the Auger electron energy distribution curve depends on E , therefore, both through the resonant Auger line shape (not central to this work) and through the PDOS.

The spectra were then broadened by applying the appropriate Lorentzian widths of about $\Gamma_{3d} + 2\Gamma_{4f}$ above resonance and $\Gamma_{3d}/2 + 2\Gamma_{4f}$ at resonance [5,26], with Γ values taken from the literature [27], plus a small allowance for experimental broadening. Interactions between the photoelectron, the Auger electron, and the core hole were explicitly not treated in the atomic calculations underpinning the Auger spectra (aside from shifts in binding energies), thereby demonstrating the validity of the sudden approximation for interpreting spectra. We also, reasonably, ignored solid-state effects on the inner-shell degrees of freedom and final state of a high kinetic-energy Auger electron.

IV. RESULTS AND DISCUSSION

The s , p , d , and f partial densities of states are shown in Fig. 3. The figure depicts the familiar broad s - p band and narrow $5d$ bands with d^{10} occupancy in Au and nominally d^9 occupancy in Pt. Above the Fermi energy (E_f), the p and f PDOS of interest for $M_{4,5}$ near-edge XAS are also shown. There is a marked crossover from the PDOS favoring p to favoring f around $E_f + 15$ eV because of the centrifugal barrier of the radial Schrödinger equation, but the f PDOS is also enhanced along with the d PDOS in the spillover of the $5d$ states above E_f in Pt.

The PDOS are similar for Au and Pt, a direct result of their face-centered cubic crystal structures and similar lattice constants and atomic structure. However, besides the $5d$ band of Pt being only nearly filled, the different lattice constants slightly change the energy scale of the XAS fine-structure oscillations [28]. The l dependence of the centrifugal barrier $l(l+1)\hbar^2/(2mr^2)$ of the radial Schrödinger equation is also readily apparent [1]: The occupied $5d$ levels lie largely above the occupied $6s$ levels, while the unoccupied $5f$ levels lie largely above the unoccupied $6p$ levels, consistent with the lower angular momentum orbitals penetrating closer to the nuclei [29]. The energy order and relative $(2l+1)$ degeneracy ($l=1$ for p states and $l=3$ for f states) accounts for the

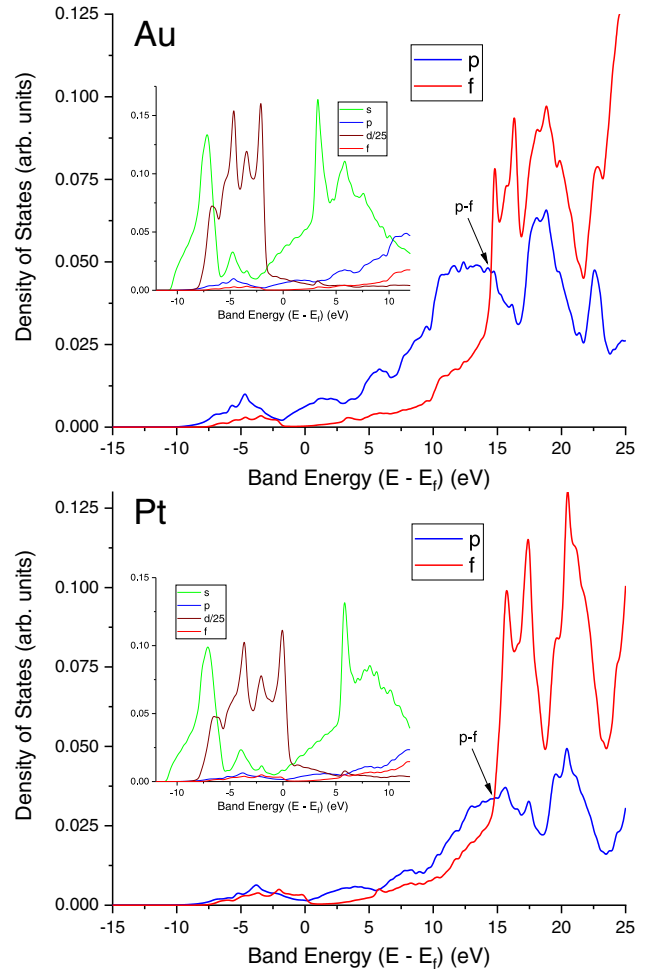


FIG. 3. Au (upper) and Pt (lower) angular-momentum-resolved LDA PDOS. The insets show the s , p , d , and f PDOS near the Fermi level, while the insets show the p and f PDOS at higher energies relevant to $3d$ photoexcitation. Note the p -to- f crossover (indicated by arrows) that occurs approximately 15 eV above the Fermi level for each.

p -to- f crossover in the unoccupied states around 15 eV above E_f . This observation is also consistent with the energy ordering of the core states: $5s$ below $4f$, below $5p$, for Au and Pt as observed in XPS spectra [30].

Figure 4 shows XAS spectra and their derivatives (*inset*) of Au and Pt around the M_5 edge. As an accurate description of the electronic structure is a prerequisite for obtaining a reliable XAS spectrum [31], the agreement between theory and experiment is consistent with our having a highly accurate unoccupied PDOS. The experimental assignment of the absorption threshold was made by determining the energy at which the $M_5N_{6,7}N_{6,7}$ Auger peak narrowed and became coincident in energy with the normal or diagram Auger line as measured above threshold [13]. This narrowing and linear dispersion of the Auger peak at threshold are hallmarks of the resonant Auger effect [5,32,33], and here we deem identification of E_f to be accurate to within 0.5 eV for both Au and Pt because the excitonic binding energies should approach zero for these well-screened metallic systems [23]. Indeed, careful

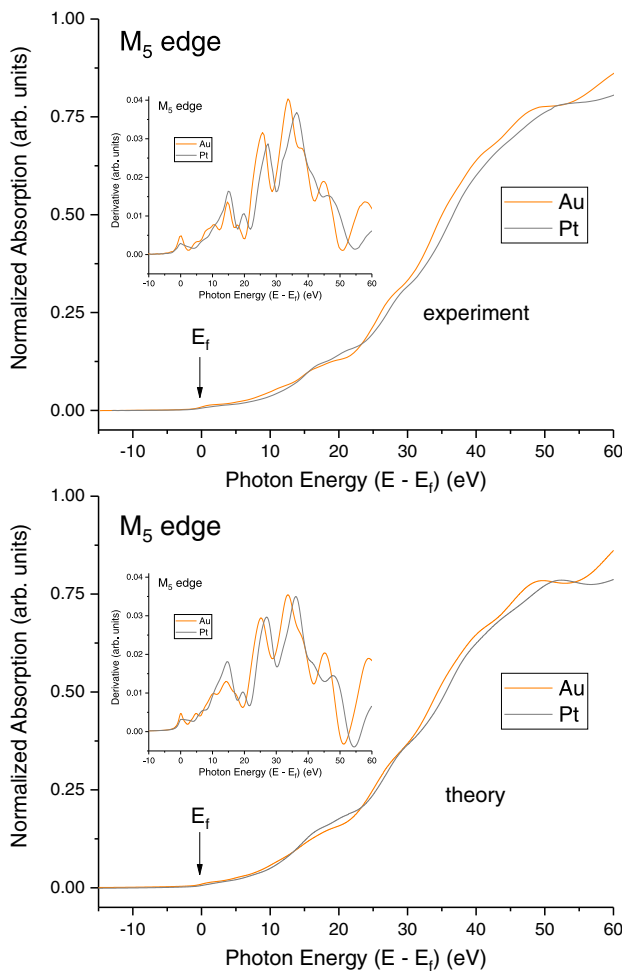


FIG. 4. Normalized M_5 XAS of Au and Pt: experiment (top); theory (bottom). The insets show their derivatives. The experimental Fermi level was determined by the resonant Auger measurements (see text).

inspection of the Auger data near threshold proved necessary for the experimental determination of E_f , which was poorly estimated by our initial XAS measurements alone. In the calculations, E_f was precisely located by electron counting and high-density Brillouin-zone sampling.

The different near-edge spectroscopic signatures of both materials are most visible in the derivatives. These differences arise from their d^{10} vs d^9 characters. Relevant to the $3d$ photoexcitation, the PDOS for Au is mostly p like, whereas for Pt it is rich in f character at E_f , as evident from the theoretical partial DOS curves. These considerations depart from prior XAS analysis where it has been convenient to overlook step-down ($l-1$) angular momentum transitions [26,34–36].

Figure 5 shows the “raw” experimental Au and Pt $M_5N_{6,7}N_{6,7}$ Auger spectra recorded as a function of photon energy above the M_5 edge. Data are shown for photon energy beginning at the M_5 resonance and continuing past the p -to- f crossover. The data have not been corrected for background; only a constant scale factor has been applied to each spectrum to make the background intensity above the Auger peaks equal to one. The “darkness” of both edges is evident in the raw Auger data.

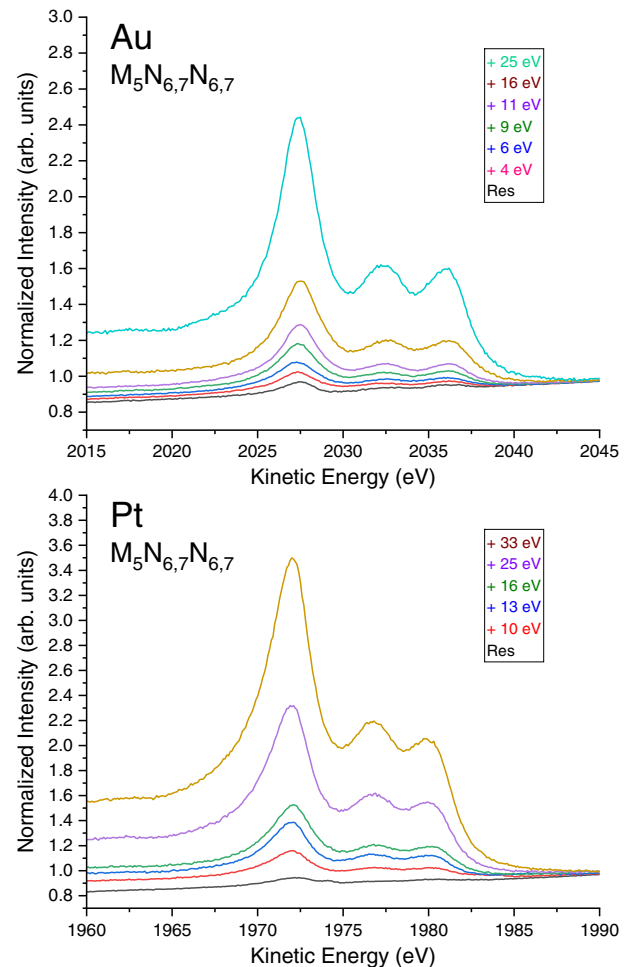


FIG. 5. As-collected Au and Pt $M_5N_{6,7}N_{6,7}$ Auger spectra recorded as a function of photon energy above the M_5 edge. The data have been multiplied only by a constant to normalize the background level at higher kinetic energy to one.

To examine the line shapes of these spectra more closely, Fig. 6 compares the $M_5N_{6,7}N_{6,7}$ Auger spectra from Fig. 5 after Shirley background subtraction [37] and normalization to equal peak height. As the Auger spectrum of a core hole is an accurate account of transitions to different $4f^{12}$ final states, these spectra and their differences are a critical test of whether the $3d$ core hole retains information contained within its j_z distribution as to how it was prepared. For both materials, the largest features of an Auger spectrum are an intense peak, accompanied by two higher-kinetic-energy lobes with approximately half the weight of the first peak. There are 91 $4f^{12}$ microstates in total [38]. The calculations reproduce many spectral features, including the significant changes observed at the p -to- f crossover. The weak feature on the low-kinetic-energy side of the Auger spectra (e.g., around 1917 eV in the Au $M_5N_{6,7}N_{6,7}$ spectrum) is associated with a 1S $4f^{12}$ multiplet level and can only result from $j_z = \pm 1/2$.

The shape of the Auger electron energy distribution curve depends on E , therefore, both through the resonant Auger line shape (not central to this work) and through the PDOS.

Figure 7 shows measured and calculated $M_4N_{6,7}N_{6,7}$ Auger spectra recorded with photon energy above the M_4 threshold

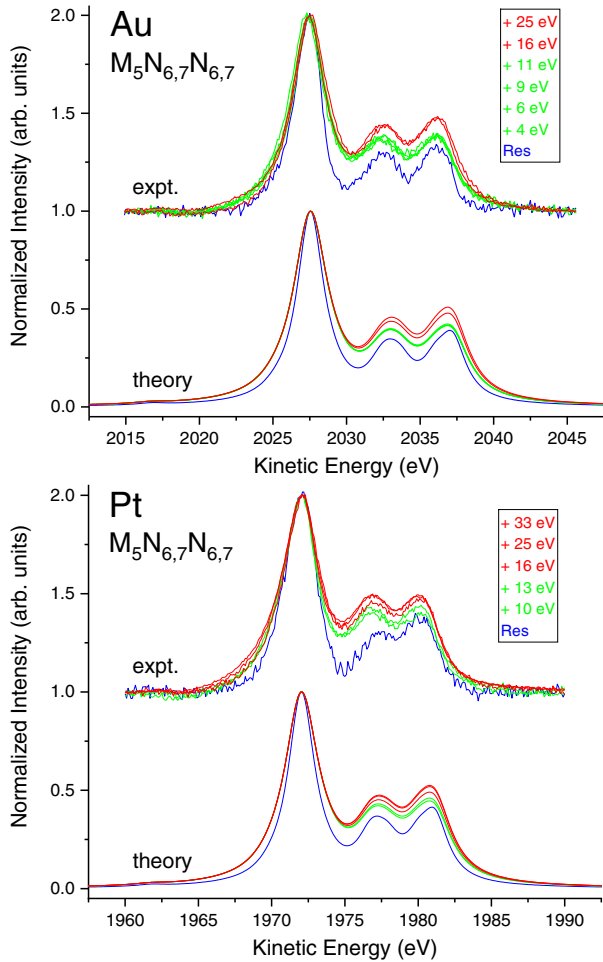


FIG. 6. Au (upper) and Pt (lower) $M_5N_{6,7}N_{6,7}$ Auger spectra as a function of photon energy above the M_5 edge. The top of each panel is the experimental data, and the bottom is the theoretical result. The spectra were normalized to have the same maximum height after Shirley background subtraction.

as indicated. Nearly full suppression of the high kinetic-energy lobe is observed for both Au and Pt relative to the $M_5N_{6,7}N_{6,7}$ spectra (Fig. 6), consistent with previous $L_{2,3}M_{4,5}M_{4,5}$ measurements for Ag, Pd, and Rh [39–43]. Differences observed here for the spin-orbit splitting of the core hole, however, emphasize Auger-transition matrix elements for filling M_5 vs M_4 core holes and not just preferential sampling of different values of core hole j_z . Nonetheless, in the M_4 case, the same four j_z values are always allowed in $d \rightarrow p$ and $d \rightarrow f$ transitions, albeit by varying amounts, and the photoexcitation-energy dependence is weak and difficult to distill. Indeed, difficulty with extracting clean Auger spectra (background subtracted, satellite free, etc.) from the data could be reasonably expected in view of the M_5 edge being only slightly lower in energy than the M_4 edge.

The work presented here is highly suitable to many current hard x-ray photoelectron spectroscopy beamlines [44], so our methodology should be of interest to much of the synchrotron radiation and electron spectroscopy community. In the past [8], others presented results for coincidence measurements of a photoelectron and Auger electron for selected emission

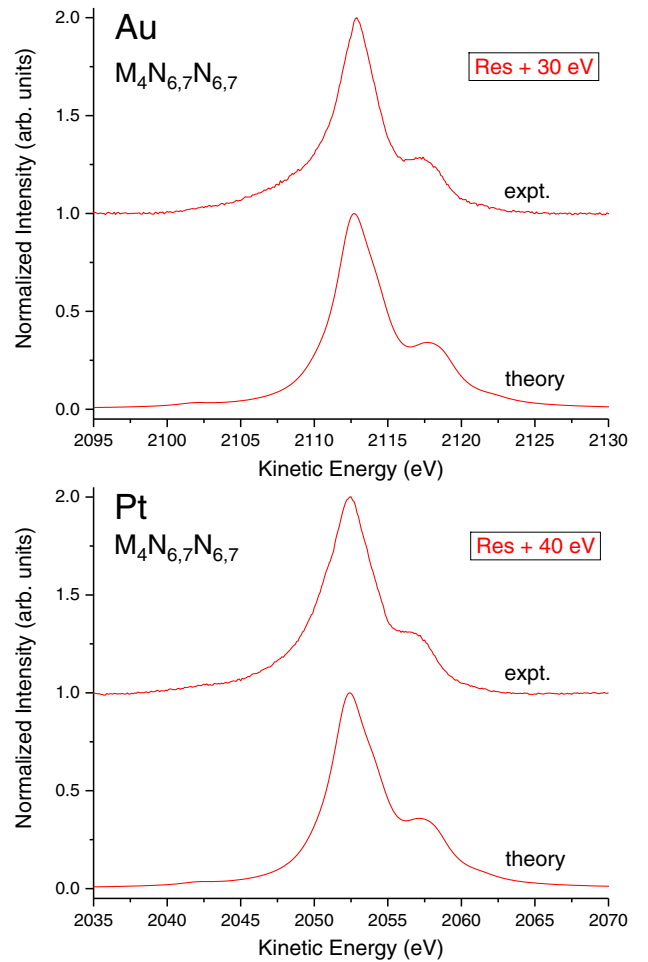


FIG. 7. Au (upper) and Pt (lower) $M_4N_{6,7}N_{6,7}$ Auger spectra for photon energies 30 or 40 eV above the M_4 resonance, respectively. The top of each panel is the experimental data, and the bottom is the theoretical result. The spectra were normalized to have the same maximum height after Shirley background subtraction.

directions at one photon energy. The work presented here differs because we do not rely on a coincidence experiment and the *multiplicity* of electron analyzers that such an experiment requires. Instead, angular selectivity is achieved using x-ray polarization and the electron analyzer acceptance cone being along the same axis, requiring only *one* electron analyzer. Additionally, our use of multiple photon energies probes different parts of the crystalline band structure and hence the different symmetries of the outgoing photoelectron.

V. CONCLUSIONS

Dark edges were observed and predicted at the $3d$ $M_{4,5}$ XAS thresholds of Au and Pt. This situation arises from angular-momentum selection rules of the dipole matrix element and the centrifugal barriers that render differentially delayed onsets of $3d \rightarrow 6p$ and $3d \rightarrow 5f$ excitations. The observation of a p -to- f PDOS crossover further restricts potentially created $3d$ holes with varying likelihoods (orbital blocking). The $M_{4,5}N_{6,7}N_{6,7}$ Auger spectra demonstrate that a $3d$ core hole directly registers how it was prepared *vis-à-vis*

the symmetry of the outgoing photoelectron final state (wave). The Zeeman-like phenomena reported here are distinct from those associated with the traditional resonant Auger effect because the latter involve Coulomb interactions between the core hole, Auger electron, and photoelectron that we have explicitly not treated. The present phenomena will also be manifest in many other systems.

Obviously, this study also showcases centrifugal-barrier effects and spectral evolution arising from the existence of multiple intermediate-state channels and final states for both photoexcitation and Auger decay. The observed effects should be quite general, because the core hole assumes quantum numbers related to those of the initially ejected photoelectron. Furthermore, the observed variations in Auger spectral features amplify the admonition that XAS measurements are reliable only insofar as a proxy signal such as electron yield is

proportional to the absorption rate, because only sampling different Auger electron energy regions would indicate different XAS spectra.

ACKNOWLEDGMENTS

This research was performed at the National Institute of Standards and Technology (NIST) beamline SST-2 of the National Synchrotron Light Source II, a U.S. Department of Energy (DOE) Office of Science User Facility operated for the DOE Office of Science by Brookhaven National Laboratory under Contract No. DE-SC0012704. J.J.R. and J.J.K. acknowledge support from DOE Office of Sciences BES Grant No. DE-FG02-97ER45623. C.A.C. acknowledges support from the NSF REU program for the summer of 2020.

-
- [1] S. Gasiorowicz, *Quantum Physics* (John Wiley and Sons, Inc., New York, 1974).
- [2] J. J. Sakurai, *Advanced Quantum Mechanics* (Addison-Wesley, London, 1967).
- [3] A. Niehaus, *J. Phys. B: At. Mol. Phys.* **10**, 1845 (1977).
- [4] J. A. de Gouw, J. van Eck, J. van der Weg, and H. G. M. Heideman, *J. Phys. B* **28**, 1761 (1995).
- [5] G. B. Armen, H. Aksela, T. Åberg, and S. Aksela, *J. Phys. B* **33**, R49 (2000).
- [6] R. Guillemin, S. Sheinerman, R. Puttner, T. Marchenko, G. Goldsztejn, L. Journel, R. K. Kushawaha, D. Ceolin, M. N. Piancastelli, and M. Simon, *Phys. Rev. A* **92**, 012503 (2015).
- [7] S. Kosugi, F. Koike, M. Iizawa, M. Oura, T. Gejo, K. Tamasaku, J. R. Harries, R. Guillemin, M. N. Piancastelli, M. Simon, and Y. Azuma, *Phys. Rev. Lett.* **124**, 183001 (2020).
- [8] R. Gotter, F. Da Pieve, A. Ruocco, F. Offi, G. Stefani, and R. A. Bartynski, *Phys. Rev. B* **72**, 235409 (2005).
- [9] C. Weiland, R. Browning, B. A. Karlin, D. A. Fischer, and J. C. Woicik, *Rev. Sci. Instrum.* **84**, 036106 (2013).
- [10] C. Weiland, A. K. Rumaiz, P. Lysaght, B. Karlin, J. C. Woicik, and D. A. Fischer, *J. Electron. Spectrosc. Relat. Phenom.* **190**, 193 (2013).
- [11] C. Weiland, C. Jaye, N. F. Quackenbush, E. Gann, Z. Fu, J. P. Kirkland, B. A. Karlin, B. Ravel, J. C. Woicik, and D. A. Fischer, *Synchrotron Radiat. News* **31**, 23 (2018).
- [12] J. C. Woicik, C. Weiland, and A. K. Rumaiz, *Phys. Rev. B* **91**, 201412(R) (2015).
- [13] J. C. Woicik, C. Weiland, A. K. Rumaiz, M. Brumbach, N. F. Quackenbush, J. M. Ablett, and E. L. Shirley, *Phys. Rev. B* **98**, 115149 (2018).
- [14] E. L. Shirley, J. Vinson, and K. Gilmore, The OCEAN suite: Core excitations, *International Tables for Crystallography* (International Union of Crystallography, 2020), Vol. I.
- [15] E. L. Shirley, L. J. Terminello, J. E. Klepeis, and F. J. Himpsel, *Phys. Rev. B* **53**, 10296 (1996).
- [16] D. R. Hamann, M. Schlüter, and C. Chiang, *Phys. Rev. Lett.* **43**, 1494 (1979).
- [17] D. Vanderbilt, *Phys. Rev. B* **32**, 8412 (1985).
- [18] A. Marini, R. Del Sole, and G. Onida, *Phys. Rev. B* **66**, 115101 (2002).
- [19] J. Vinson, J. J. Rehr, J. J. Kas, and E. L. Shirley, *Phys. Rev. B* **83**, 115106 (2011).
- [20] K. Gilmore, J. Vinson, E. L. Shirley, D. Prendergast, C. D. Pemmaraju, J. J. Kas, F. D. Vila, and J. J. Rehr, *Comput. Phys. Comm.* **197**, 109 (2015).
- [21] J. Vinson and E. L. Shirley, *Phys. Rev. B* **103**, 245143 (2021).
- [22] M. Abramowitz and I. Stegun, *Handbook of Mathematical Functions* (United States Government Printing Office, Washington, DC, 1964).
- [23] O. Madelung, *Introduction to Solid-State Theory* (Springer-Verlag, Berlin, 1981).
- [24] E. L. Shirley, Ph.D. thesis, University of Illinois at Urbana-Champaign, 1991.
- [25] D. D. Koelling and B. N. Harmon, *J. Phys. C: Solid State Phys.* **10**, 3107 (1977).
- [26] W. Drube, R. Treusch, and G. Materlik, *Phys. Rev. Lett.* **74**, 42 (1995).
- [27] J. L. Campbell and T. Papp, *At. Data Nucl. Data Tables* **77**, I (2001).
- [28] J. J. Rehr and R. C. Albers, *Rev. Mod. Phys.* **72**, 621 (2000).
- [29] M. Karplus and R. N. Porter, *Atoms and Molecules: An Introduction for Students of Physical Chemistry* (The Benjamin Cummings Publishing Company, Menlo Park, CA, 1970).
- [30] C. D. Wanger, W. M. Riggs, L. E. Davis, J. F. Moulder, and G. E. Muilenberg, *Handbook of X-ray Photoelectron Spectroscopy: A Reference Book of Standard Spectra for Identification and Interpretation of XPS Data* (Perkin-Elmer Corp., Physical Electronics Division, Eden Prairie, MN, 1979).
- [31] H.-P. Komsa and A. V. Krashennnikov, *Phys. Rev. B* **86**, 241201(R) (2012).
- [32] G. S. Brown, M. H. Chen, B. Crasemann, and G. E. Ice, *Phys. Rev. Lett.* **45**, 1937 (1980).
- [33] G. B. Armen, T. Åberg, J. C. Levin, B. Crasemann, M. H. Chen, G. E. Ice, and G. S. Brown, *Phys. Rev. Lett.* **54**, 1142 (1985).
- [34] T. K. Sham, *Phys. Rev. B* **31**, 1888 (1985).
- [35] L. J. P. Ament, M. van Veenendaal, T. P. Devereaux, J. P. Hill, and J. van den Brink, *Rev. Mod. Phys.* **83**, 705 (2011).

- [36] P. H. Citrin, *Phys. Rev. B* **31**, 700 (1985).
- [37] D. A. Shirley, *Phys. Rev. B* **5**, 4709 (1972).
- [38] P. L. Meena, N. Kumar, A. S. Meena, K. S. Meena, and P. K. Jain, *Bulg. Chem. Commun.* **45**, 388 (2013).
- [39] E. Antonides, E. C. Janse, and G. A. Sawatzky, *Phys. Rev. B* **15**, 1669 (1977).
- [40] P. Weightman, P. T. Andrews, and A. C. Parry-Jones, *J. Phys. C: Solid State Phys.* **12**, 3635 (1979).
- [41] S. L. Sorensen, R. Carr, S. J. Schaphorst, S. B. Whitfield, and B. Crasemann, *Phys. Rev. A* **39**, 6241 (1989).
- [42] G. G. Kleiman, R. Landers, and S. G. C. de Castro, *J. Electron. Spectrosc. Relat. Phenom.* **68**, 329 (1994).
- [43] A. M. Ferraria, A. P. Carapeto, and A. M. Botelho do Rego, *Vacuum* **86**, 1988 (2012).
- [44] *Hard X-Ray Photoelectron Spectroscopy (HAXPES)*, edited by J. C. Woicik (Springer, Berlin, 2016).